



LAWRENCE  
LIVERMORE  
NATIONAL  
LABORATORY

# An energy absorbing far-field boundary condition for the elastic wave equation

N. A. Petersson, B. Sjogreen

July 16, 2008

Communications in Computational Physics

## **Disclaimer**

---

This document was prepared as an account of work sponsored by an agency of the United States government. Neither the United States government nor Lawrence Livermore National Security, LLC, nor any of their employees makes any warranty, expressed or implied, or assumes any legal liability or responsibility for the accuracy, completeness, or usefulness of any information, apparatus, product, or process disclosed, or represents that its use would not infringe privately owned rights. Reference herein to any specific commercial product, process, or service by trade name, trademark, manufacturer, or otherwise does not necessarily constitute or imply its endorsement, recommendation, or favoring by the United States government or Lawrence Livermore National Security, LLC. The views and opinions of authors expressed herein do not necessarily state or reflect those of the United States government or Lawrence Livermore National Security, LLC, and shall not be used for advertising or product endorsement purposes.

# An Energy Absorbing Far-Field Boundary Condition for the Elastic Wave Equation

N. Anders Petersson and Björn Sjögreen

July 15, 2008

## Abstract

We present an energy absorbing non-reflecting boundary condition of Clayton-Engquist type for the elastic wave equation together with a discretization which is stable for any ratio of compressional to shear wave speed. We prove stability for a second order accurate finite-difference discretization of the elastic wave equation in three space dimensions together with a discretization of the proposed non-reflecting boundary condition. The stability proof is based on a discrete energy estimate and is valid for heterogeneous materials. The proof includes all six boundaries of the computational domain where special discretizations are needed at the edges and corners. The stability proof holds also when a free surface boundary condition is imposed on some sides of the computational domain.

## 1 Introduction

In regional simulations of seismic wave propagation, the extent of the computational domain must be limited to make the problem computationally tractable. Some form of far-field absorbing boundary condition needs to be imposed where the computational domain is truncated such that waves can propagate out of the computational domain without being reflected due to the artificial boundary. For a material with constant wave speeds, and a domain with a single planar boundary, it is possible to derive a boundary condition which allows all waves to exit the domain without any artificial reflection. However, such a boundary condition involves a pseudo-differential operator and is therefore non-local in space and unsuitable for numerical computations.

One of the first practically useful far-field boundary condition for the elastic wave equation was derived by Clayton and Engquist [4], where the authors presented a hierarchy of boundary conditions by approximating the exact pseudo-differential operator to increasing order of accuracy in the angle of incidence. (All boundary conditions in the hierarchy are perfectly non-reflecting for waves of normal incidence.) A slightly different approach was suggested by Higdon in [9], where the boundary condition is obtained by component wise application of a scalar non-reflecting boundary condition. Higdon also derived a hierarchy of boundary conditions with increasingly absorbing properties. In the

case of a scalar wave equation, the Higdon and Clayton-Engquist boundary conditions are equivalent. First order Clayton-Engquist conditions have been used extensively in large scale computations of seismic wave propagation, see [5]. However, instabilities have been reported for the third order condition for some values of the wave speeds [12].

The perfectly matched layer (PML) is a more modern boundary condition which was originally developed for Maxwell's equations by Berenger [2] and has been studied in numerous subsequent papers, see for example [16] and the references therein. Perfectly matched layers have superior non-reflecting properties compared to low order Clayton-Engquist or Higdon conditions, but they are also more complicated to implement and require correct tuning of the size and strength of the absorbing layer. PML's for the elastic wave equation were developed in [10, 1]. Unfortunately, interaction with material discontinuities leading to surface waves can cause the PML boundary condition to become unstable [17].

Higdon [8] performed a normal-mode stability analysis for a class of discretized non-reflecting boundary conditions for the elastic wave equation, which includes the first order Clayton-Engquist condition as a special case. In particular, Higdon showed stability for a first order accurate discretization of the Clayton-Engquist condition. Note that the normal mode analysis is only valid for half-space problems with homogeneous materials and does not take corners or edges into account. Furthermore, the stability concept in the normal mode analysis only guarantees the solution to be bounded independently of the grid size for a fixed, finite, interval in time. It does not exclude the possibility that the solution may grow as the time interval is made longer. We remark that the discretization given in the original paper by Clayton and Engquist [4] is second order accurate and is therefore not covered by Higdon's analysis.

In seismic simulations, the material properties are not known very precisely and there are often uncertainties associated with the source terms modeling the spatial distribution and temporal variation of the slip during an earthquake. We therefore believe that in many realistic seismic simulations, adequate accuracy can be obtained by using low order outflow boundary conditions as long as they are stable. Often the material properties vary rapidly on the computational grid and this can cause stability problems for the Clayton-Engquist conditions, which are derived under the assumption of constant coefficients. Additional stability problems occur for large ratios between the compressional and shear wave speeds:  $c_p/c_s$ . Here,

$$c_p = \sqrt{\frac{2\mu + \lambda}{\rho}}, \quad c_s = \sqrt{\frac{\mu}{\rho}},$$

where  $\mu$ ,  $\lambda$  are the Lamé parameters and  $\rho$  is density.

In this paper we propose an alternative non-reflecting boundary condition based on summation by part operators, which is stable for all values of  $c_p/c_s$ . Since the stability follows from an energy estimate for the fully discretized problem, the proposed boundary condition is stable in realistic situations with strongly variable coefficients and our theory includes edges and corners of a logically cubical three-dimensional domain.

When implementing a production code for use by application experts, who often do not have expertise in tuning numerical stabilizing parameters, we believe it is extremely valuable to use techniques where there is a mathematical proof of the stability of the

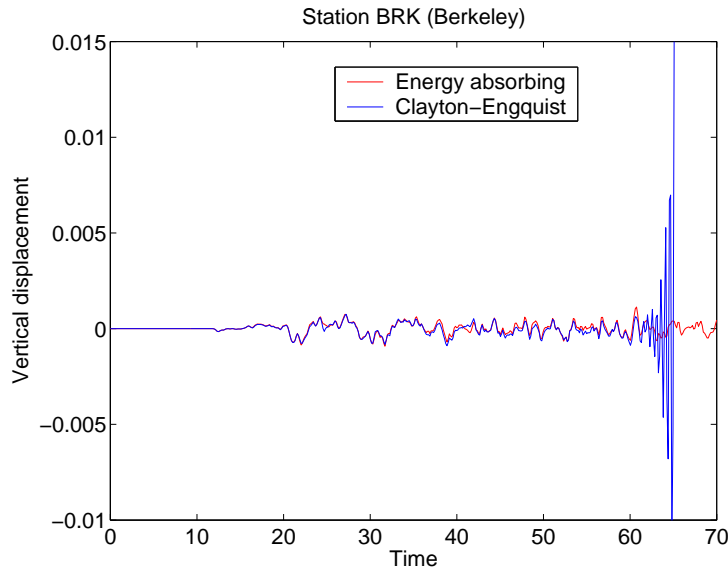


Figure 1: Simulation of the October, 2007, Alum Rock earthquake using the Clayton-Engquist (blue) and energy absorbing (red) boundary conditions.

underlying numerical method. Hence, the main advantage of the method proposed in this article lies in the stability proof for heterogeneous materials including corners and edges. Furthermore, the stability follows from an energy estimate which shows that the energy is bounded as time goes to infinity on a fixed grid.

While the Clayton-Engquist condition works well in most practical situations, there are cases where it makes the simulation go unstable. The instability appears to occur when the outflow boundary cuts through a heterogeneous material with high  $c_p/c_s$  ratio. As a motivating example, consider the synthetic seismograms in Figure 1 from two simulations of the magnitude 5.4 earthquake which occurred in Alum Rock, CA, in October of 2007. Both calculations were performed using the WPP code [15] and a modified version of the material model from the U.S. Geological Survey [3]. The first, displayed in blue, uses the first order Clayton-Engquist non-reflecting boundary condition. This computation is unstable and the solution starts growing exponentially after time  $\approx 60$  seconds. The second computation, displayed in red, uses the stable energy absorbing non-reflecting boundary condition proposed in this paper. In this case the solution remains bounded for long times.

The remainder of this paper is organized in the following way. In Section 2 we review the standard non-reflecting boundary conditions and present the basic idea behind our proposed boundary condition. Furthermore, we investigate reflection properties for various non-reflecting boundary conditions in the continuous setting. In Section 3 we introduce a discretization of the elastic wave equation together with the proposed non-reflecting boundary conditions, and prove that this approximation satisfies a discrete energy estimate. Finally, in Section 4 we show some numerical examples where our proposed boundary condition is compared to the first order Clayton-Engquist condition.

## 2 Absorbing boundary conditions

The elastic wave equation can be formulated in terms of the displacement vector  $\mathbf{u}(\mathbf{x}, t) = (u(\mathbf{x}, t), v(\mathbf{x}, t), w(\mathbf{x}, t))^T$  where  $\mathbf{x} = (x, y, z)^T$  is the Cartesian coordinate and  $t$  is time,

$$\rho \mathbf{u}_{tt} = \operatorname{div} \mathcal{T}(\mathbf{u}) + \mathbf{f}(\mathbf{x}, t), \quad \mathbf{x} \in \Omega, \quad t \geq 0. \quad (1)$$

Here  $\rho = \rho(\mathbf{x}) > 0$  is the density,  $\mathbf{f}(\mathbf{x}, t)$  is the external forcing, and  $\mathcal{T}(\mathbf{u})$  is the stress tensor,

$$\mathcal{T}(\mathbf{u}) = \lambda \operatorname{div}(\mathbf{u}) I + 2\mu \mathcal{D}(\mathbf{u}).$$

The Lamé parameters  $\mu(\mathbf{x}) > 0$  and  $\lambda(\mathbf{x}) > 0$  characterize the elastic properties of the material. The identity matrix is denoted by  $I$ , and the symmetric part of the displacement gradient is given by

$$\mathcal{D}(\mathbf{u}) = \frac{1}{2} \begin{pmatrix} 2u_x & u_y + v_x & u_z + w_x \\ u_y + v_x & 2v_y & v_z + w_y \\ u_z + w_x & v_z + w_y & 2w_z \end{pmatrix}.$$

The displacement and its first time derivative are given as initial data, and boundary conditions are enforced along the boundary of the domain,  $\partial\Omega$ .

### 2.1 Clayton-Engquist's hierarchy of far-field boundary conditions

Consider the case where the boundary is the plane  $x = 0$  and  $\Omega$  is the half-space  $x > 0$ ,  $-\infty < y < \infty$ ,  $-\infty < z < \infty$ . Freeze the coefficients of (1) and cast it into the form

$$\mathbf{u}_{tt} = A\mathbf{u}_{xx} + B\mathbf{u}_{xy} + C\mathbf{u}_{yy} + D\mathbf{u}_{zz} + E\mathbf{u}_{xz} + F\mathbf{u}_{yz}. \quad (2)$$

Fourier transformation in space and time with dual variables  $t \rightarrow \omega$ ,  $x \rightarrow k_x$ ,  $y \rightarrow k_y$ , and  $z \rightarrow k_z$  gives the algebraic relation

$$0 = -I + A \frac{k_x^2}{\omega^2} + \frac{k_x k_y}{\omega} B + \frac{k_y^2}{\omega^2} C + \frac{k_z^2}{\omega^2} D + \frac{k_x k_z}{\omega} E + \frac{k_y k_z}{\omega} F =: P \left( \frac{k_x}{\omega}, \frac{k_y}{\omega}, \frac{k_z}{\omega} \right). \quad (3)$$

We define the  $p$ 'th order Clayton-Engquist non-reflecting boundary condition as the differential equation obtained by inverse Fourier transformation of

$$\frac{k_x}{\omega} = C_{00} + \sum_{q=1}^{n-1} \sum_{l=1}^{n-1} \left( \frac{k_y}{\omega} \right)^q \left( \frac{k_z}{\omega} \right)^l C_{ql}. \quad (4)$$

Here the matrix  $C_{00}$  has positive eigenvalues, and the matrices  $C_{ql}$  are determined to make

$$P \left( \frac{k_x}{\omega}, \frac{k_y}{\omega}, \frac{k_z}{\omega} \right) = \mathcal{O} \left( \left( \frac{k_y}{\omega} \right)^p + \left( \frac{k_z}{\omega} \right)^p \right), \quad (5)$$

when the ansatz (4) is inserted into (3). Note that the  $p$ 'th order non-reflecting boundary condition is not unique, because the number of terms  $n$  can be chosen larger than necessary to satisfy (5). If the smallest possible number of terms in (5) is used, we call the resulting boundary condition a minimal  $p$ 'th order Clayton-Engquist condition.

In general, the matrices  $C_{ql}$  have coefficients that depend on the compressional wave speed,  $c_p$ , and the shear wave speed,  $c_s$ . For example

$$C_{00} = \begin{pmatrix} 1/c_p & 0 & 0 \\ 0 & 1/c_s & 0 \\ 0 & 0 & 1/c_s \end{pmatrix}.$$

It follows that the minimal first order Clayton-Engquist boundary condition for the half-plane problem  $x > 0$  is

$$\begin{aligned} u_t &= c_p u_x, \\ v_t &= c_s v_x, \quad x = 0, \quad t \geq 0, \\ w_t &= c_s w_x. \end{aligned} \tag{6}$$

## 2.2 Energy absorbing boundary conditions

When the external forcing is zero,  $\mathbf{f}(\mathbf{x}, t) = 0$ , the following energy estimate holds for (1),

$$\frac{1}{2} \frac{d}{dt} \left( \|\rho^{1/2} \mathbf{u}_t\|^2 + \int_{\Omega} \lambda (\operatorname{div} \mathbf{u})^2 + 2\mu (D : D) d\mathbf{x} \right) = \int_{\partial\Omega} \mathbf{u}_t^T \mathcal{T}(\mathbf{u}) \mathbf{n} dS. \tag{7}$$

Here  $\mathbf{n}$  is the outward unit normal of the boundary,  $dS$  is a surface element, and tensor contraction over two indices is defined by

$$(A : B) = \sum_{i=1}^3 \sum_{j=1}^3 a_{i,j} b_{i,j}.$$

According to (7), any boundary condition that satisfies

$$\mathbf{u}_t^T \mathcal{T}(\mathbf{u}) \mathbf{n} \leq 0, \quad \mathbf{x} \in \partial\Omega, \quad t \geq 0, \tag{8}$$

leads to non-increasing energy in the solution and thereby a well-posed problem. Examples of boundary conditions satisfying (8) with an equality are the free surface boundary condition  $\mathcal{T}(\mathbf{u}) \mathbf{n} = \mathbf{0}$  and the homogeneous Dirichlet condition  $\mathbf{u} = \mathbf{0}$ . Both these condition are non-dissipative. In general any boundary condition of the form

$$\mathbf{u}_t = -M \mathcal{T}(\mathbf{u}) \mathbf{n}, \quad \mathbf{x} \in \partial\Omega, \quad t \geq 0, \tag{9}$$

where  $M$  is a positive definite matrix, is dissipative because it makes the right hand side of (7) negative.

We can make (9) agree with the first order Clayton-Engquist conditions in the normal direction by taking

$$M = \frac{1}{\sqrt{\rho}} \begin{pmatrix} 1/\sqrt{2\mu + \lambda} & 0 & 0 \\ 0 & 1/\sqrt{\mu} & 0 \\ 0 & 0 & 1/\sqrt{\mu} \end{pmatrix},$$

which defines our proposed boundary condition in the continuous setting. For the half-space problem ( $x > 0$ ) in Section 2.1,  $\mathbf{n} = (-1, 0, 0)^T$  on  $x = 0$ , and the proposed boundary condition becomes

$$\begin{aligned} u_t &= c_p u_x + \frac{\lambda}{\sqrt{\rho(2\mu + \lambda)}}(v_y + w_z), \\ v_t &= c_s v_x + c_s u_y, \\ w_t &= c_s w_x + c_s u_z. \end{aligned} \quad x = 0, \quad t \geq 0, \quad (10)$$

This boundary condition belongs to the class of Clayton-Engquist conditions of order  $p = 1$  with  $n = 2$ . The key difference compared to the minimal first order Clayton-Engquist condition (6) is that the right hand side of boundary condition (10) is proportional to the normal stresses along the boundary. Energy estimate (7) can therefore be used to show that (10) is energy absorbing, both for constant and variable coefficients ( $\rho, \lambda, \mu$ ).

## 2.3 Reflection properties

In this section we compare the reflection properties of the continuous (no discretization) minimal Clayton-Engquist boundary conditions of order  $p = 1, 2, 3$  and the proposed boundary condition (10). To simplify the presentation, we only consider the two-dimensional elastic wave equation in the  $(x, y)$ -plane. We consider the half-plane domain  $x > 0$ ,  $-\infty < y < \infty$ , where an incident planar wave starting at infinity travels at an angle  $0 \leq \theta \leq \pi/2$  from the negative  $x$ -direction. Ideally this wave should pass through the  $x = 0$  boundary without reflections. In practice, the wave gets partially reflected when  $\theta \neq 0$  and some energy travels back into the  $x > 0$  half-plane. The reflected wave consists of both an  $S$ -wave and a  $P$ -wave. We therefore obtain four different reflection coefficients: 1) reflected  $P$ -wave from incident  $P$ -wave, 2) reflected  $S$ -wave from incident  $P$ -wave, 3) reflected  $P$ -wave from incident  $S$ -wave, and 4) reflected  $S$ -wave from incident  $S$ -wave. Furthermore, the reflection coefficients can become complex valued, indicating an evanescent reflected wave.

The general solution for  $x > 0$  with an incident  $P$ -wave and reflection coefficients  $R_{pp}$  and  $R_{ps}$  is

$$\mathbf{u}(x, y, t) = e^{i(\omega t + k_x x + k_y y)} \begin{pmatrix} k_x \\ k_y \end{pmatrix} + R_{pp} e^{i(\omega t - k_x x + k_y y)} \begin{pmatrix} k_x \\ k_y \end{pmatrix} + \frac{R_{ps} e^{i(\omega t - \alpha k_x x + k_y y)}}{\sqrt{\alpha^2 k_x^2 + k_y^2}} \begin{pmatrix} -k_y \\ \alpha k_x \end{pmatrix}, \quad (11)$$

where  $k_x^2 + k_y^2 = 1$ ,  $\omega = c_p$ , and  $\alpha$  is chosen to make  $c_s^2(\alpha^2 k_x^2 + k_y^2) = c_p^2$ .



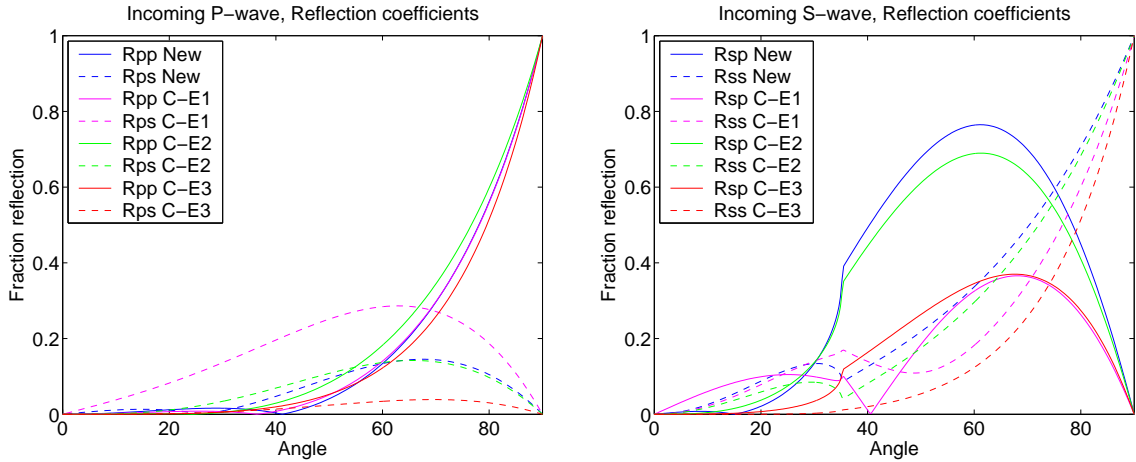


Figure 2: Reflection coefficients when  $c_p/c_s = 1.732$ . Incident  $P$ -wave (left) and incident  $S$ -wave (right). Solid curves are  $P$  wave reflections and dashed curves are  $S$  wave reflections.

We determine the reflection coefficients by inserting (11) into the outflow boundary condition, such as the two-dimensional counterparts of (10) or (6). In two space dimensions, two boundary equations give two linear equations for the unknowns  $R_{pp}$  and  $R_{ps}$ . For an incident  $S$ -wave, we insert the corresponding general solution into the outflow boundary condition to determine the reflection coefficients  $R_{sp}, R_{ss}$ .

Figure 2 shows the absolute value of the reflection coefficients  $|R_{pp}|$  (solid curves) and  $|R_{ps}|$  (dashed curves) for the proposed energy absorbing condition (10) (blue) and the minimal Clayton-Engquist conditions of orders one (purple), two (green), and three (red), when the ratio of wave speeds equals  $c_p/c_s = 1.732$ . The case of incident  $S$ -wave (right subfigure), have complex reflection coefficients when the incident angle is larger than 35 degrees.

In Figure 3 we show the same reflection coefficients as in Figure 2, for the case  $c_p/c_s = 30$ . In the case of an incoming  $S$ -wave, note that the reflection coefficients are in many cases greater than one. However, the reflection coefficients of the proposed boundary condition (10) are always less than unity.

These results raise some concerns about the well-posedness of the Clayton-Engquist boundary conditions for high ratios  $c_p/c_s$ , also for the lowest order conditions. However, the first order minimal Clayton-Engquist condition has been shown to be well-posed, in two space dimensions, for all ratios  $c_p/c_s > 0$ , see [8]. Note that for the first order minimal condition, the only amplification occurs for a  $P$  wave that is reflected from an incident  $S$  wave. Because the  $P$  wave can not be amplified further by new reflections, it can not grow unlimitedly due to repeated reflections. Engquist [6] proved that the third order condition is well-posed if  $c_p/c_s < 2$ . Our results indicate that the third order condition is ill-posed for  $c_p/c_s > 2$ . The instability for the third order condition when  $c_p/c_s > 2$  has been demonstrated in numerical experiments [12].

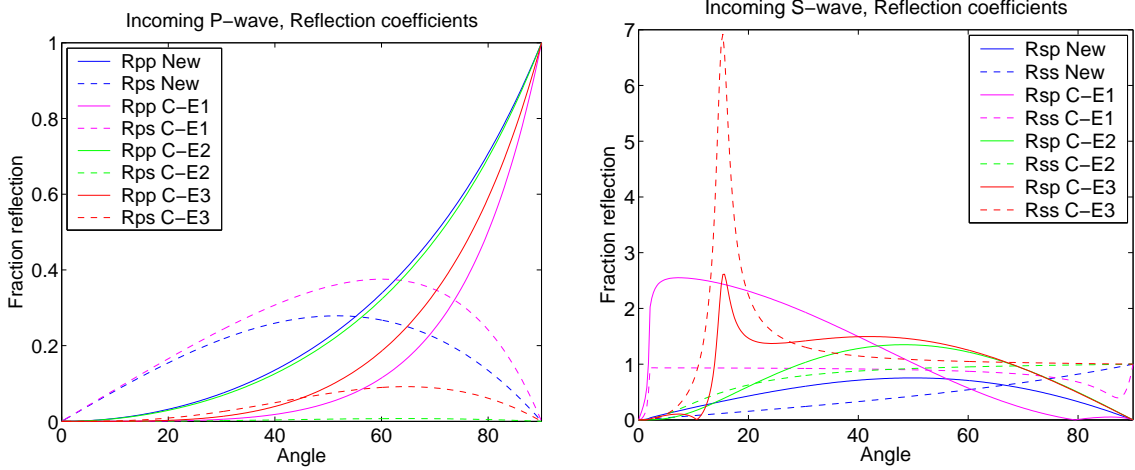


Figure 3: Reflection coefficients when  $c_p/c_s = 30$ . Incident  $P$ -wave (left) and incident  $S$ -wave (right). Solid curves are  $P$  wave reflections and dashed curves are  $S$  wave reflections.

### 3 Stable discretizations of the elastic wave equation

We discretize the elastic wave equation (1) on the domain  $0 \leq x \leq a$ ,  $0 \leq y \leq b$ ,  $0 \leq z \leq c$ . On the boundaries we either impose the free surface condition  $\mathcal{T}(\mathbf{u}) \mathbf{n} = \mathbf{0}$ , or the proposed energy absorbing condition (10).

We introduce a grid spacing  $h > 0$ , a time step  $\Delta t > 0$ , and consider the finite difference approximation of (1),

$$\rho_{i,j,k} \frac{\mathbf{u}_{i,j,k}^{n+1} - 2\mathbf{u}_{i,j,k}^n + \mathbf{u}_{i,j,k}^{n-1}}{\Delta t^2} = \mathbf{L}(\mathbf{u})_{i,j,k} + \mathbf{f}_{i,j,k}(t_n), \quad (12)$$

where we used the vector notation  $\mathbf{u} = (u, v, w)^T$  and  $\mathbf{L}(\mathbf{u})_{i,j,k}$  represents the discretization of the spatial operator in (1). The external forcing is discretized according to

$$\mathbf{f}_{i,j,k}(t) = (f_{i,j,k}^{(u)}(t), f_{i,j,k}^{(v)}(t), f_{i,j,k}^{(w)}(t))^T = \mathbf{f}(\mathbf{x}_{i,j,k}, t).$$

Let the grid function  $u_{i,j,k}^n$  denote the approximation of the  $x$ -component of the displacement at grid point  $x_i = (i-1)h$ ,  $y_j = (j-1)h$ ,  $z_k = (k-1)h$  and at time  $t_n = n\Delta t$ . In the same way,  $v_{i,j,k}^n$  and  $w_{i,j,k}^n$  denote the approximations of the  $y$ - and  $z$ -components of the displacement, respectively. The domain sizes and the grid spacing are defined such that  $x_{N_x} = a$ ,  $y_{N_y} = b$ , and  $z_{N_z} = c$ . The discrete equation (12) is applied at grid points  $1 \leq i \leq N_x$ ,  $1 \leq j \leq N_y$ , and  $1 \leq k \leq N_z$ . The grid points with  $i = 0$ ,  $i = N_x + 1$ ,  $j = 0$ ,  $j = N_y + 1$ ,  $k = 0$ , or  $k = N_z + 1$  are called ghost points, and are used to impose the boundary conditions.

We generalize the summation by parts discretization introduced in [14] to include boundary modified mixed derivatives on all six sides of the domain. In component form, the spatial discretization is given by

$$\mathbf{L}(\mathbf{u}) = (L^{(u)}(u, v, w), L^{(v)}(u, v, w), L^{(w)}(u, v, w))^T,$$

where

$$\begin{aligned} L^{(u)}(u, v, w) = & D_-^x (E_{1/2}^x(2\mu + \lambda)D_+^x u) + D_-^y (E_{1/2}^y(\mu)D_+^y u) + D_-^z (E_{1/2}^z(\mu)D_+^z u) \\ & + \widetilde{D}_0^x (\lambda \widetilde{D}_0^y v + \lambda \widetilde{D}_0^z w) + \widetilde{D}_0^y (\mu \widetilde{D}_0^x v) + \widetilde{D}_0^z (\mu \widetilde{D}_0^x w), \end{aligned} \quad (13)$$

$$\begin{aligned} L^{(v)}(u, v, w) = & D_-^x (E_{1/2}^x(\mu)D_+^x v) + D_-^y (E_{1/2}^y(2\mu + \lambda)D_+^y v) + D_-^z (E_{1/2}^z(\mu)D_+^z v) \\ & + \widetilde{D}_0^x (\mu \widetilde{D}_0^y u) + \widetilde{D}_0^y (\lambda \widetilde{D}_0^x u + \lambda \widetilde{D}_0^z w) + \widetilde{D}_0^z (\mu \widetilde{D}_0^y w), \end{aligned} \quad (14)$$

$$\begin{aligned} L^{(w)}(u, v, w) = & D_-^x (E_{1/2}^x(\mu)D_+^x w) + D_-^y (E_{1/2}^y(\mu)D_+^y w) + D_-^z (E_{1/2}^z(2\mu + \lambda)D_+^z w) \\ & + \widetilde{D}_0^x (\mu \widetilde{D}_0^z u) + \widetilde{D}_0^y (\mu \widetilde{D}_0^z v) + \widetilde{D}_0^z (\lambda \widetilde{D}_0^x u + \lambda \widetilde{D}_0^y v). \end{aligned} \quad (15)$$

Here we used the standard second order accurate divided difference operators, i.e.,

$$D_+^x u_{i,j,k} = (u_{i+1,j,k} - u_{i,j,k})/h, \quad D_-^x u_{i,j,k} = D_+^x u_{i-1,j,k}, \quad D_0^x = \frac{1}{2}(D_+^x + D_-^x).$$

The boundary modified operator defining differences in the  $x$ -direction is defined by

$$\widetilde{D}_0^x u_{i,j,k} = \begin{cases} D_+^x u_{i,j,k}, & i = 1, \\ D_0^x u_{i,j,k}, & 2 \leq i \leq N_x - 1, \\ D_-^x u_{i,j,k}, & i = N_x, \end{cases}$$

and the averaging operator is defined by

$$E_{1/2}^x(\mu)_{i,j,k} = \frac{1}{2} (\mu_{i+1,j,k} + \mu_{i,j,k}).$$

The superscripts on the difference and averaging operators denote the direction in which the operator is applied and we use corresponding definitions for the difference operators in the  $y$ - and  $z$ -directions.

To analyze the stability of the discrete equations, we define the weighted scalar product,

$$(u, v)_h = h^3 \sum_{i=1}^{N_x} \sum_{j=1}^{N_y} \sum_{k=1}^{N_z} a_i^{(x)} a_j^{(y)} a_k^{(z)} u_{i,j,k} v_{i,j,k},$$

where the weights satisfy

$$a_i^{(x)} = \begin{cases} 1/2, & i = 1 \text{ or } i = N_x, \\ 1, & 1 < i < N_x, \end{cases}$$

with corresponding definitions of  $a^{(y)}$  and  $a^{(z)}$ . We define the vector scalar product and norm by

$$(\mathbf{u}^0, \mathbf{u}^1)_h = (u^0, u^1)_h + (v^0, v^1)_h + (w^0, w^1)_h, \quad \|\mathbf{u}\|_h^2 = (\mathbf{u}, \mathbf{u})_h.$$

To discretize the boundary conditions, we use a special approximation of the stress tensor on the boundary which matches the properties of the boundary modified discretization of the cross terms in (13)-(15). On the sides  $I = 1$  and  $I = N_x$ ,

$$\begin{aligned} (\mathcal{B}_{I,j,k}^n)^{11} &= \frac{1}{2}(2\mu + \lambda)_{I-1/2,j,k} D_-^x u_{I,j,k}^n + \frac{1}{2}(2\mu + \lambda)_{I+1/2,j,k} D_+^x u_{I,j,k}^n \\ &\quad + \lambda_{I,j,k} (\widetilde{D}_0^y v_{I,j,k}^n + \widetilde{D}_0^z w_{I,j,k}^n), \\ (\mathcal{B}_{I,j,k}^n)^{21} &= \frac{1}{2}\mu_{I-1/2,j,k} D_-^x v_{I,j,k}^n + \frac{1}{2}\mu_{I+1/2,j,k} D_+^x v_{I,j,k}^n + \mu_{I,j,k} \widetilde{D}_0^y u_{I,j,k}^n, \\ (\mathcal{B}_{I,j,k}^n)^{31} &= \frac{1}{2}\mu_{I-1/2,j,k} D_-^x w_{I,j,k}^n + \frac{1}{2}\mu_{I+1/2,j,k} D_+^x w_{I,j,k}^n + \mu_{I,j,k} \widetilde{D}_0^z u_{I,j,k}^n. \end{aligned} \quad (16)$$

The stress components on the sides  $J = 1$  and  $J = N_y$  are discretized as

$$\begin{aligned} (\mathcal{B}_{i,J,k}^n)^{12} &= \frac{1}{2}\mu_{i,J-1/2,k} D_-^y u_{i,J,k}^n + \frac{1}{2}\mu_{i,J+1/2,k} D_+^y u_{i,J,k}^n + \mu_{i,J,k} \widetilde{D}_0^x v_{i,J,k}^n, \\ (\mathcal{B}_{i,J,k}^n)^{22} &= \frac{1}{2}(2\mu + \lambda)_{i,J-1/2,k} D_-^y v_{i,J,k}^n + \frac{1}{2}(2\mu + \lambda)_{i,J+1/2,k} D_+^y v_{i,J,k}^n \\ &\quad + \lambda_{i,J,k} (\widetilde{D}_0^x u_{i,J,k}^n + \widetilde{D}_0^z w_{i,J,k}^n), \\ (\mathcal{B}_{i,J,k}^n)^{32} &= \frac{1}{2}\mu_{i,J-1/2,k} D_-^y w_{i,J,k}^n + \frac{1}{2}\mu_{i,J+1/2,k} D_+^y w_{i,J,k}^n + \mu_{i,J,k} \widetilde{D}_0^z v_{i,J,k}^n. \end{aligned} \quad (17)$$

and the stress components on the sides  $K = 1$  and  $K = N_z$  are discretized as

$$\begin{aligned} (\mathcal{B}_{i,j,K}^n)^{13} &= \frac{1}{2}\mu_{i,j,K-1/2} D_-^z u_{i,j,K}^n + \frac{1}{2}\mu_{i,j,K+1/2} D_+^z u_{i,j,K}^n + \mu_{i,j,K} \widetilde{D}_0^x w_{i,j,K}^n, \\ (\mathcal{B}_{i,j,K}^n)^{23} &= \frac{1}{2}\mu_{i,j,K-1/2} D_-^z v_{i,j,K}^n + \frac{1}{2}\mu_{i,j,K+1/2} D_+^z v_{i,j,K}^n + \mu_{i,j,K} \widetilde{D}_0^y w_{i,j,K}^n, \\ (\mathcal{B}_{i,j,K}^n)^{33} &= \frac{1}{2}(2\mu + \lambda)_{i,j,K-1/2} D_-^z w_{i,j,K}^n + \frac{1}{2}(2\mu + \lambda)_{i,j,K+1/2} D_+^z w_{i,j,K}^n \\ &\quad + \lambda_{i,j,K} (\widetilde{D}_0^x u_{i,j,K}^n + \widetilde{D}_0^y v_{i,j,K}^n). \end{aligned} \quad (18)$$

Our main result is given in the following theorem:

**Theorem 1** *The approximation (12) with  $\mathbf{f} = \mathbf{0}$  satisfies a discrete energy estimate under a CFL restriction on  $\Delta t/h$  if the discretization of the boundary conditions satisfies*

$$(\mathbf{u}_{i,j,k}^{n+1} - \mathbf{u}_{i,j,k}^{n-1})^T \mathcal{B}_{i,j,k}^n \mathbf{n}_{i,j,k} \leq 0, \quad (\text{no summation over } i, j, k), \quad (19)$$

on all faces of the boundary. Here,

$$\mathcal{B}_{i,j,k}^n = \begin{pmatrix} (\mathcal{B}_{i,j,k}^n)^{11} & (\mathcal{B}_{i,j,k}^n)^{12} & (\mathcal{B}_{i,j,k}^n)^{13} \\ (\mathcal{B}_{i,j,k}^n)^{21} & (\mathcal{B}_{i,j,k}^n)^{22} & (\mathcal{B}_{i,j,k}^n)^{23} \\ (\mathcal{B}_{i,j,k}^n)^{31} & (\mathcal{B}_{i,j,k}^n)^{32} & (\mathcal{B}_{i,j,k}^n)^{33} \end{pmatrix},$$

and  $\mathbf{n}_{i,j,k}$  is the outward boundary normal. (For example,  $\mathbf{n}_{1,j,k} = (-1, 0, 0)^T$  on the boundary with  $i = 1$  and  $\mathbf{n}_{i,j,N_z} = (0, 0, 1)^T$  on the boundary with  $k = N_z$ .)

**Remark:** The free surface boundary conditions and the Dirichlet conditions used in [14] satisfy (19) with equality.

The proof of Theorem 1 relies on the following fundamental identity.

**Lemma 1** *For any two vector grid functions  $\mathbf{u}^0$  and  $\mathbf{u}^1$  it holds that*

$$(\mathbf{u}^1, \mathbf{L}(\mathbf{u}^0))_h = -S(\mathbf{u}^1, \mathbf{u}^0) + T(\mathbf{u}^1, \mathbf{u}^0), \quad (20)$$

where  $S$  is symmetric and positive semi-definite, i.e.,  $S(\mathbf{u}^1, \mathbf{u}^0) = S(\mathbf{u}^0, \mathbf{u}^1)$  and  $S(\mathbf{u}, \mathbf{u}) \geq 0$  for all  $\mathbf{u}$ . Furthermore,  $S(\mathbf{u}^0, \mathbf{u}^1)$  is a function of the interior points only, no ghost points appear in the expression for  $S(\mathbf{u}^0, \mathbf{u}^1)$ . The non-symmetric boundary term is given by

$$\begin{aligned} T(\mathbf{u}^1, \mathbf{u}^0) = & h^2 \sum_{j=1}^{N_y} \sum_{k=1}^{N_z} a_j^{(y)} a_k^{(z)} \left( (\mathbf{u}_{1,j,k}^1)^T \mathcal{B}_{1,j,k}^0 \mathbf{n}_{1,j,k} + (\mathbf{u}_{N_x,j,k}^1)^T \mathcal{B}_{N_x,j,k}^0 \mathbf{n}_{N_x,j,k} \right) \\ & + h^2 \sum_{i=1}^{N_x} \sum_{k=1}^{N_z} a_i^{(x)} a_k^{(z)} \left( (\mathbf{u}_{i,1,k}^1)^T \mathcal{B}_{i,1,k}^0 \mathbf{n}_{i,1,k} + (\mathbf{u}_{i,N_y,k}^1)^T \mathcal{B}_{i,N_y,k}^0 \mathbf{n}_{i,N_y,k} \right) \\ & + h^2 \sum_{i=1}^{N_x} \sum_{j=1}^{N_y} a_i^{(x)} a_j^{(y)} \left( (\mathbf{u}_{i,j,1}^1)^T \mathcal{B}_{i,j,1}^0 \mathbf{n}_{i,j,1} + (\mathbf{u}_{i,j,N_z}^1)^T \mathcal{B}_{i,j,N_z}^0 \mathbf{n}_{i,j,N_z} \right). \end{aligned} \quad (21)$$

**Proof:** See Appendix A.

We define the discrete energy

$$E^{n+1} = \left\| \rho^{1/2} \frac{\mathbf{u}^{n+1} - \mathbf{u}^n}{\Delta t} \right\|_h^2 - (\mathbf{u}^{n+1}, \mathbf{L}(\mathbf{u}^n))_h + T(\mathbf{u}^{n+1}, \mathbf{u}^n) \quad (22)$$

The discrete counterpart of the energy estimate (7) is given by

**Lemma 2** *In the absence of external forcing,  $\mathbf{f}(t)=0$ , the discrete energy satisfies*

$$E^{n+1} - E^n = T(\mathbf{u}^{n+1} - \mathbf{u}^{n-1}, \mathbf{u}^n).$$

**Proof:** At each grid point  $(i, j, k)$  with  $1 \leq i \leq N_x$ ,  $1 \leq j \leq N_y$ , and  $1 \leq k \leq N_z$  the difference scheme (12) can be written

$$\frac{\rho}{\Delta t^2} (\mathbf{u}^{n+1} - \mathbf{u}^n) - \frac{\rho}{\Delta t^2} (\mathbf{u}^n - \mathbf{u}^{n-1}) = \mathbf{L}(\mathbf{u}^n). \quad (23)$$

Point wise scalar multiplication by  $(\mathbf{u}^{n+1} - \mathbf{u}^{n-1})$  gives

$$\frac{\rho}{\Delta t^2} (\mathbf{u}^{n+1} - \mathbf{u}^{n-1})^T (\mathbf{u}^{n+1} - \mathbf{u}^n) - \frac{\rho}{\Delta t^2} (\mathbf{u}^{n+1} - \mathbf{u}^{n-1})^T (\mathbf{u}^n - \mathbf{u}^{n-1}) = (\mathbf{u}^{n+1} - \mathbf{u}^{n-1})^T \mathbf{L}(\mathbf{u}^n).$$

After some algebra, we get

$$\begin{aligned} & \frac{\rho}{\Delta t^2} (\mathbf{u}^{n+1} - \mathbf{u}^n)^T (\mathbf{u}^{n+1} - \mathbf{u}^n) - (\mathbf{u}^{n+1})^T \mathbf{L}(\mathbf{u}^n) \\ & - \frac{\rho}{\Delta t^2} (\mathbf{u}^n - \mathbf{u}^{n-1})^T (\mathbf{u}^n - \mathbf{u}^{n-1}) + (\mathbf{u}^n)^T \mathbf{L}(\mathbf{u}^{n-1}) = (\mathbf{u}^n)^T \mathbf{L}(\mathbf{u}^{n-1}) - (\mathbf{u}^{n-1})^T \mathbf{L}(\mathbf{u}^n). \end{aligned}$$

Point wise multiplication by the weights  $a^{(x)}a^{(y)}a^{(z)}$  and summation over all non-ghost grid points give

$$\begin{aligned} \left\| \frac{\mathbf{u}^{n+1} - \mathbf{u}^n}{\Delta t} \rho^{1/2} \right\|_h^2 - (\mathbf{u}^{n+1}, \mathbf{L}(\mathbf{u}^n))_h - \left\| \frac{\mathbf{u}^n - \mathbf{u}^{n-1}}{\Delta t} \rho^{1/2} \right\|_h^2 + (\mathbf{u}^n, \mathbf{L}(\mathbf{u}^{n-1}))_h \\ = (\mathbf{u}^n, \mathbf{L}(\mathbf{u}^{n-1}))_h - (\mathbf{u}^{n-1}, \mathbf{L}(\mathbf{u}^n))_h, \end{aligned}$$

and we arrive at

$$E^{n+1} - E^n = (\mathbf{u}^n, \mathbf{L}(\mathbf{u}^{n-1}))_h - (\mathbf{u}^{n-1}, \mathbf{L}(\mathbf{u}^n))_h + T(\mathbf{u}^{n+1}, \mathbf{u}^n) - T(\mathbf{u}^n, \mathbf{u}^{n-1}).$$

The symmetry properties of Lemma 1 give

$$(\mathbf{u}^n, \mathbf{L}(\mathbf{u}^{n-1}))_h - (\mathbf{u}^{n-1}, \mathbf{L}(\mathbf{u}^n))_h = T(\mathbf{u}^n, \mathbf{u}^{n-1}) - T(\mathbf{u}^{n-1}, \mathbf{u}^n),$$

and therefore

$$E^{n+1} - E^n = -T(\mathbf{u}^{n-1}, \mathbf{u}^n) + T(\mathbf{u}^{n+1}, \mathbf{u}^n) = T(\mathbf{u}^{n+1} - \mathbf{u}^{n-1}, \mathbf{u}^n),$$

which proves the lemma.  $\square$

Lemma 2 shows that the discrete energy is non-increasing ( $E^{n+1} \leq E^n$ ) if and only if the boundary inequality (19) is satisfied.

The final step in our stability proof is to show that the discrete energy always is non-negative. Lemma 1 defines the symmetric positive semi-definite quadratic form

$$S(\mathbf{u}, \mathbf{v}) = -(\mathbf{u}, \mathbf{L}(\mathbf{v}))_h + T(\mathbf{u}, \mathbf{v}).$$

**Lemma 3** *The energy is non-negative,*

$$E^n \geq 0,$$

for all  $n \geq 0$  if the CFL-condition  $\zeta_{\max} \Delta t^2 \leq 4$  holds, where

$$\zeta_{\max} = \max_{\mathbf{u} \neq \mathbf{0}} \frac{S(\mathbf{u}, \mathbf{u})}{(\rho \mathbf{u}, \mathbf{u})_h}. \quad (24)$$

**Proof:** The symmetry of  $S(\mathbf{u}, \mathbf{v})$  gives

$$\begin{aligned} E^{n+1} &= \left\| \rho^{1/2} \frac{\mathbf{u}^{n+1} - \mathbf{u}^n}{\Delta t} \right\|_h^2 + \frac{1}{2} S(\mathbf{u}^{n+1}, \mathbf{u}^n) + \frac{1}{2} S(\mathbf{u}^n, \mathbf{u}^{n+1}) \\ &= \left\| \rho^{1/2} \frac{\mathbf{u}^{n+1} - \mathbf{u}^n}{\Delta t} \right\|_h^2 - \frac{1}{4} S(\mathbf{u}^{n+1} - \mathbf{u}^n, \mathbf{u}^{n+1} - \mathbf{u}^n) + \frac{1}{4} S(\mathbf{u}^{n+1} + \mathbf{u}^n, \mathbf{u}^{n+1} + \mathbf{u}^n). \end{aligned} \quad (25)$$

Since  $S(\mathbf{u}^{n+1} + \mathbf{u}^n, \mathbf{u}^{n+1} + \mathbf{u}^n) \geq 0$ ,  $E^{n+1} \geq 0$  if

$$\frac{1}{\Delta t^2} \|\rho^{1/2} \mathbf{w}\|_h^2 - \frac{1}{4} S(\mathbf{w}, \mathbf{w}) \geq 0, \quad (26)$$

for all  $\mathbf{w} = \mathbf{u}^{n+1} - \mathbf{u}^n$ . Clearly, (26) holds if  $\mathbf{w} = \mathbf{0}$ . If  $\mathbf{w} \neq \mathbf{0}$ , we rewrite (26) as

$$\frac{\Delta t^2}{4} \frac{S(\mathbf{w}, \mathbf{w})}{(\rho \mathbf{w}, \mathbf{w})_h} \leq 1,$$

which shows the lemma.  $\square$

**Proof of Theorem 1:** Lemma 2 and (21) show that condition (19) leads to a non-increasing energy. Furthermore, Lemma 3 shows that the energy is non-negative under the CFL-condition (24). Hence, we arrive at the energy estimate

$$0 \leq E^n \leq E^{n-1} \leq \dots \leq E^0,$$

which proves the theorem.  $\square$

### 3.1 Discrete non-reflecting boundary conditions

We here present the discretization of our proposed boundary condition (10) which satisfies (19). To simplify the presentation, we focus on the boundary where  $i = 1$ ,

$$\begin{aligned} \frac{u_{1,j,k}^{n+1} - u_{1,j,k}^{n-1}}{2\Delta t} &= \frac{(\mathcal{B}_{1,j,k}^n)^{11}}{\sqrt{\rho_{1,j,k}(2\mu + \lambda)_{1,j,k}}}, \\ \frac{v_{1,j,k}^{n+1} - v_{1,j,k}^{n-1}}{2\Delta t} &= \frac{(\mathcal{B}_{1,j,k}^n)^{21}}{\sqrt{\rho_{1,j,k}\mu_{1,j,k}}}, \\ \frac{w_{1,j,k}^{n+1} - w_{1,j,k}^{n-1}}{2\Delta t} &= \frac{(\mathcal{B}_{1,j,k}^n)^{31}}{\sqrt{\rho_{1,j,k}\mu_{1,j,k}}}. \end{aligned} \quad (27)$$

Thus the boundary condition is imposed at the grid points  $(1, j, k)$ , where we also impose the internal difference scheme (12). The ghost point values at the new time level,  $\mathbf{u}_{0,j,k}^{n+1}$ , do not appear in (27), but are instead determined such that (12) and (27) give the same value for  $\mathbf{u}_{1,j,k}^{n+1}$ . For example, for the first equation in (27) we solve

$$2u_{1,j,k}^n - u_{1,j,k}^{n-1} + \frac{\Delta t^2}{\rho_{1,j,k}} L^{(u)}(u^n, v^n, w^n)_{1,j,k} + f_{1,j,k}^{(u)} = u_{1,j,k}^{n-1} + \frac{2\Delta t (\mathcal{B}_{1,j,k}^n)^{11}}{\sqrt{\rho_{1,j,k}(2\mu + \lambda)_{1,j,k}}} \quad (28)$$

for the ghost point value  $u_{0,j,k}^n$ , which occurs in  $L^{(u)}(u^n, v^n, w^n)_{1,j,k}$  and  $(\mathcal{B}_{1,j,k}^n)^{11}$ . Equation (28) can be written of the form  $\alpha u_{0,j,k}^n = \beta$ , where  $\alpha \neq 0$  and  $\beta$  is a function of the solution at the interior grid points at  $t_n$  and  $t_{n-1}$ . We determine  $v_{0,j,k}^n$  and  $w_{0,j,k}^n$  similarly.

At an edge of the domain where two boundary conditions of the type (27) meet, for example at the grid points  $(1, 1, k)$ , we use the same technique to obtain a coupled linear system of two equations for the two unknowns  $u_{0,1,k}^n$  and  $u_{1,0,k}^n$ . Similarly, at a corner where three sides with boundary conditions of the type (27) meet, we obtain a coupled linear system of three equations for three unknowns, e.g.,  $u_{0,1,1}^n$ ,  $u_{1,0,1}^n$ ,  $u_{1,1,0}^n$ .

The ghost point values can be solved for directly along boundary faces where the free surface condition is imposed. For example, if the boundary with  $k = 1$  is a free surface, we enforce the discrete boundary conditions

$$(\mathcal{B}_{i,j,1}^n)^{13} = (\mathcal{B}_{i,j,1}^n)^{23} = (\mathcal{B}_{i,j,1}^n)^{33} = 0. \quad (29)$$

These equations obviously satisfy (19), and it is evident from (18) that the ghost point values  $u_{i,j,0}^n$ ,  $v_{i,j,0}^n$ ,  $w_{i,j,0}^n$  do not couple along the boundary or to other boundaries along the edges.

## 4 Numerical experiments

To numerically investigate the outflow boundary conditions we discretize the elastic wave equation in three space dimensions by the formulas (12)–(15). The free surface boundary condition is discretized by (29), the energy absorbing boundary condition by (27), and the minimal first order Clayton-Engquist condition by the technique suggested in [4], except for edges and corners which are treated according to [14]. On boundaries with Clayton-Engquist conditions, a centered approximation replaces the boundary modified operators for mixed derivatives in (13)–(15) (i.e.,  $\widetilde{D}_0^x$  is replaced by  $D_0^x$ , etc.).

All experiments were run with version 1.2 of the open source code WPP [15], which solves the elastic wave equation in the setting of seismic applications. WPP implements all combinations of energy absorbing, free surface, Clayton-Engquist as well as Dirichlet boundary conditions, including all special cases for edges and corners in three spatial dimensions.

### 4.1 Influence of $c_p/c_s$ ratio on stability

To verify the energy absorbing property of our proposed boundary condition and to investigate how the ratio  $c_p/c_s$  influences the performance of the far field boundary conditions, we consider the elastic wave equation on the domain  $[0, 2] \times [0, 2] \times [0, 2]$ . A homogeneous free surface condition is imposed at  $z = 0$  and far field boundary conditions are imposed on all other boundaries. The external forcing is set to zero, i.e.,  $\mathbf{f} = \mathbf{0}$  in (12). Throughout this experiment we use a random number generator  $\theta$  which gives uniformly distributed values between zero and one, where the sequence is determined by a seed number. We first use the random number generator to assign initial data. By writing  $\mathbf{u}_{i,j,k}^0 = \theta$  and  $\mathbf{u}_{i,j,k}^{-1} = \theta$  we mean that the random number generator is invoked separately for each component of the displacement, each grid point, at each time level to generate an extremely unsmooth displacement field.

We consider the two cases  $c_p/c_s = 1.732 \approx \sqrt{3}$  and  $c_p/c_s = 30$ . When  $c_p/c_s = 1.732$  we run the computation to time  $t = 20$  with CFL number 0.7, corresponding to 926 time steps. When  $c_p/c_s = 30$ , the time step is smaller and we run the computation to time  $t = 2$  with CFL number 0.7, giving 1244 time steps. For both ratios of  $r = c_p/c_s$ , we use two different materials. First we use a homogeneous material with  $\mu = 2.5$ ,  $\lambda = \mu(r^2 - 2)$ ,  $\rho = 2.5$ . Secondly, we use the random number generator  $\theta$  to create a material with extremely unsmooth spatial variation:  $\mu = 2 + \theta$ ,  $\lambda = \mu(r^2 - 2) + \theta$ , and  $\rho = 2 + \theta$ .

Figure 4 displays the energy (22) as function of time for the minimal first order Clayton-Engquist (CE1) and energy absorbing (EA) far field boundary condition, respectively. In the case of the Clayton-Engquist condition, the boundary term  $T$  is excluded from (22) since it is not relevant. We show results for both the homogeneous randomly varying materials. The left subplot of Figure 4 displays results for the wave speed ratio  $c_p/c_s = 1.732$ , while the right hand subplot of Figure 4 shows the case  $c_p/c_s = 30$ . For the lower  $c_p/c_s$  ratio, the energy absorbing and Clayton-Engquist boundary conditions behave similarly. However, only the energy absorbing boundary condition performs well for the larger  $c_p/c_s$  ratio, whereas the Clayton-Engquist condition is unstable. Note that the behavior is similar for both constant and random materials.



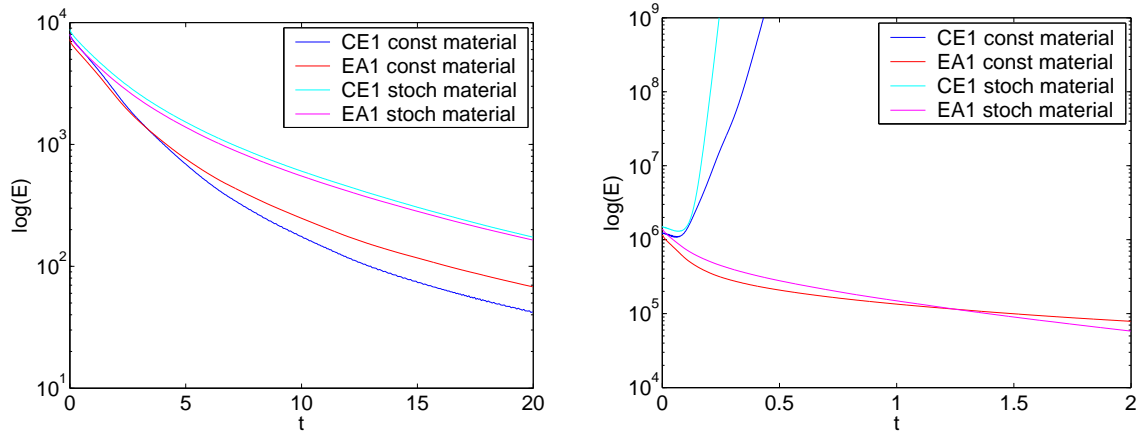


Figure 4: Logarithm of energy vs. time when  $c_p/c_s = 1.732$  (left) and when  $c_p/c_s = 30$  (right). Random initial data. Constant material (blue and red curves) and randomly varying material (cyan and magenta curves).

In Figure 5 we show the energy difference  $E^{n+1} - E^n$  as function of time for the energy absorbing boundary condition when  $c_p/c_s = 30$  with the randomly varying material. Note that the energy is perfectly decreasing, as expected from our theory.

## 4.2 Lamb's problem with $\lambda = \mu$

Lamb [11] derived an analytic solution to the elastic wave equation in a homogeneous half-space subject to an impulsive point forcing on the free surface boundary. Many generalizations have been made to Lamb's original derivation, see for example [13] or [7]. Here we focus on the case with  $\lambda = \mu$  (Poisson ratio 1/4) which simplifies the evaluation of the analytic solution.

We solve Lamb's problem numerically on the truncated domain  $0 \leq x \leq 12$ ,  $0 \leq y \leq 12$ ,  $0 \leq z \leq 6$  with the point force

$$\mathbf{f}(\mathbf{x}, t) = \begin{pmatrix} 0 \\ 0 \\ g(t)\delta(\mathbf{x} - \mathbf{x}_0) \end{pmatrix},$$

where  $\delta(\mathbf{x} - \mathbf{x}_0)$  is the Dirac distribution centered at  $\mathbf{x}_0 = (6, 6, 0)$  and

$$g(t) = \begin{cases} 1024t^5(1 - 5t + 10t^2 - 10t^3 + 5t^4 - t^5), & 0 < t < 1, \\ 0, & \text{otherwise.} \end{cases}$$

The function  $g(t)$ , displayed in Figure 6, is four times continuously differentiable. The smoothness in time of the point forcing translates to smoothness in space of the solution after the point force has stopped acting, i.e., for times  $t > 1$  in this case. Far field boundary conditions are enforced on all sides of the domain except along  $z = 0$ , where

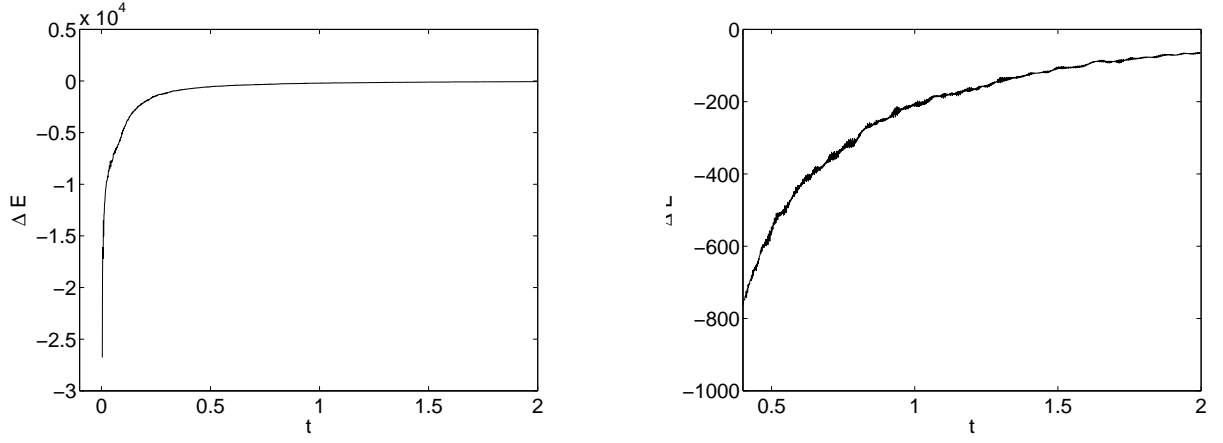


Figure 5: Energy difference  $E^{n+1} - E^n$  as function of time when  $c_p/c_s = 30$  for the energy absorbing boundary condition. Both subfigures show the same curve, but the scale on the vertical axis goes from  $-3 \times 10^4$  to  $5 \times 10^2$  in the left subplot, and from -1000 to 0 in the right subplot.

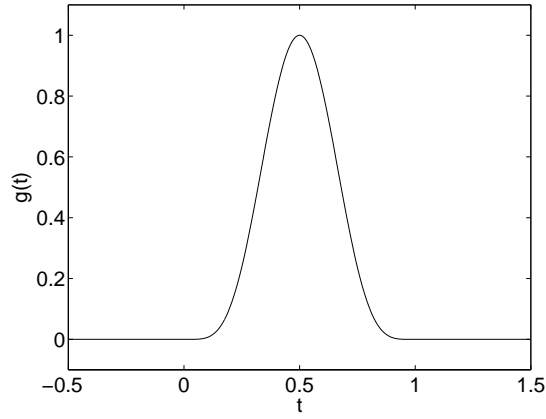


Figure 6: Time dependency of source function,  $g(t)$ , used in Lamb's problem.

the discretized free surface condition (29) is imposed. The material has the constant properties  $\mu = \lambda = \rho = 1$ , which implies that  $c_p/c_s = \sqrt{3}$ .

Figure 7 shows the numerical solution at three different times when the energy absorbing far field boundary condition is used. The plotted quantity is the magnitude of the displacement,  $\sqrt{u^2 + v^2 + w^2}$ . The point forcing on the surface initiates a strong Rayleigh surface wave. A weak downward propagating compressional wave moving with speed  $c_p = \sqrt{3}$  can be seen in the top left and right subfigures, before it exits the computational domain. The shear wave moves with speed  $c_s = 1$  and consequently arrives at the bottom of the domain near time 6, as can be seen in the middle right subfigure. It can be shown that the Rayleigh surface wave propagates with phase velocity  $c_r \approx 0.92$  when  $\mu = \lambda$ , so the surface wave should reach the corners of the  $z = 0$  plane at  $t \approx 9.22$ , which agrees well with the bottom left subfigure. The only visible wave in the bottom right subfigure, as indicated by the first contour level at 0.00375, is an artifact of the far-field boundary condition. These artifacts get more pronounced near the corners of the  $z = 0$  plane, as can be seen in the bottom left subfigure.

The evolution of the solution along the surface is shown in more detail in Figure 8. Here we study the magnitude of the displacement as function of  $x$ , along the line  $z = 0$ ,  $y = 6$ . The solution is dominated by the Rayleigh surface wave and its decaying amplitude is due to geometrical spreading along the  $z = 0$  surface. The surface wave travels with phase velocity  $c_r \approx 0.92$ , so the wave arrives at the outflow boundary at  $t \approx 6.52$ . While most of the wave is transmitted through the outflow boundary, it is apparent that some of it gets reflected back into the computational domain, even though the surface wave has normal incidence to the boundary along this line. This behavior is explained by the mismatch in phase velocity between the surface waves and shear waves, because the outflow boundary condition only provides perfect transmission of waves at normal incidence when they travel at the shear or compressional phase velocities.

The error in the numerical solution of Lamb's problem has contributions from the numerical discretization of the governing equations as well as errors due to the truncation of the computational domain. The numerical discretization error can further be divided into errors due to the discretization of the elastic wave equation, the discretization of the free surface boundary condition, and the discrete approximation of the point force. Because the analytical solution is very hard to evaluate in the interior of the domain, we limit our study to evaluating the error in the  $z$ -component of the solution along the boundary  $z = 0$ . For this purpose we define the maximum and  $L_2$ -norm on the surface by

$$||w||_\infty = \max_{i,j}(|w_{i,j,1}|), \quad ||w||_2 = \sqrt{h^2 \sum_{j=1}^{N_y} \sum_{i=1}^{N_x} w_{i,j,1}^2}.$$

In Table 1 we display the error in the numerical solution at time 3 for three different grid sizes. Because no waves have reached the far-field boundary at this time, these errors are solely due to effects of the numerical discretization. Table 1 illustrates that the errors decrease with decreasing grid size, at close to the expected second order convergence rate. Table 2 displays errors in the maximum norm along the  $z = 0$  surface at time 11, comparing the influence of either the minimal first order Clayton-Engquist, energy absorbing, or homogeneous Dirichlet boundary conditions on the far-field boundaries.

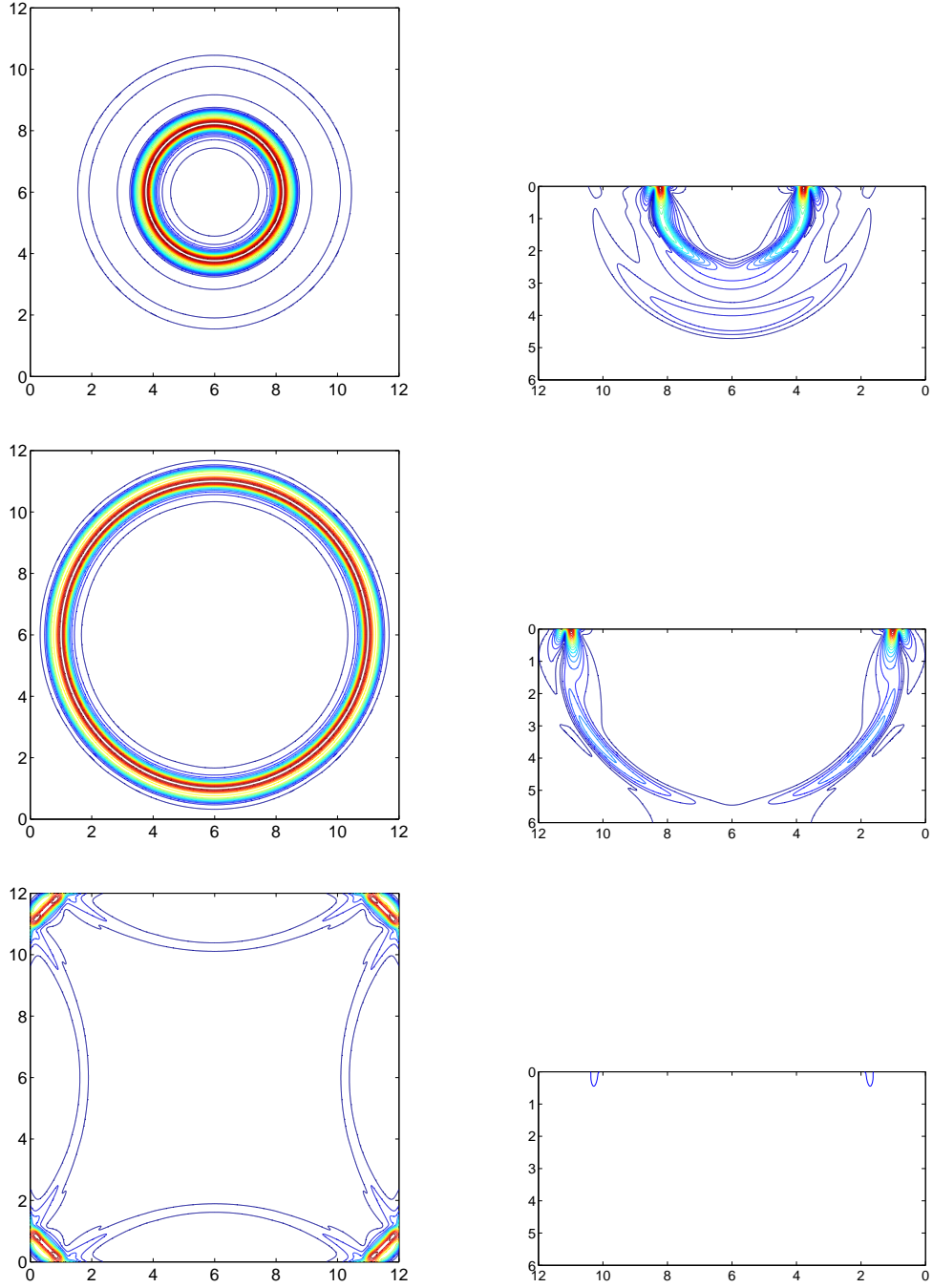


Figure 7: Magnitude of the displacement for Lamb's problem at times 3, 6, and 9 (from top to bottom) in the  $z = 0$  plane (left) and  $y = 6$  plane (right). The energy absorbing far-field boundary condition (27) was used to truncate the computational domain in this calculation, which used the grid size  $h = 0.02$ . The contour levels are the same in all plots and are equally spaced between 0 and 0.15 with interval 0.00375.

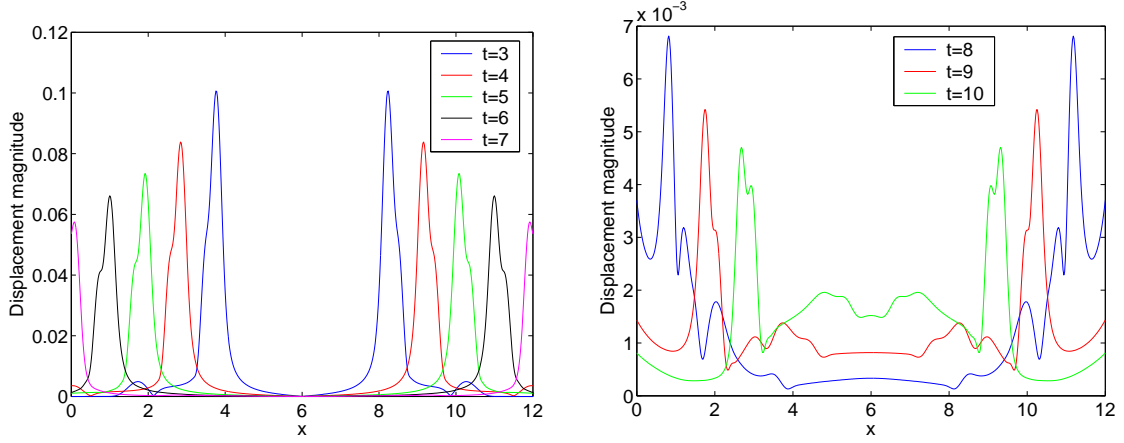


Figure 8: Magnitude of the surface displacement in the numerical solution of Lamb's problem when the energy absorbing far-field boundary condition (27) is used to truncate the computational domain. The displacement is shown as function of  $x$ , along the line  $z = 0$ ,  $y = 6$ , at times 3, 4, 5, 6, 7 (left) and times 8, 9, 10 (right). Note that the vertical scale goes from 0 to 0.12 on the left, but from 0 to  $7 \times 10^{-3}$  on the right.

$h$	$L^\infty$ error	$L^2$ error	$L^\infty$ ratio	$L^2$ ratio
0.04	0.01192	0.02406	*	*
0.02	0.00374	0.00751	3.18	3.20
0.01	0.00100	0.00201	3.74	3.74

Table 1: Errors in the  $w$  component of the solution along the surface  $z = 0$  for Lamb's problem when  $c_p/c_s = \sqrt{3}$  at time 3, before any waves have reached the far-field boundaries.

$h$	CE1	Energy Absorbing	Dirichlet
0.04	0.00313	0.00813	0.07467
0.02	0.00356	0.00947	0.08360

Table 2: Maximum norm errors in the  $w$  component of the solution along the surface  $z = 0$  for Lamb’s problem when  $c_p/c_s = \sqrt{3}$  at time 11, after all waves in the exact solution have exited the computational domain.

Setting the displacement to zero on the far-field boundary causes significant reflections so the Dirichlet boundary conditions are only provided as a reference point. Note that all waves should have exited the computational domain at this time, so the exact solution is identically zero inside the computational domain. In this case the errors are almost independent of the grid size, which indicates that the error is dominated by effects of the far-field boundary condition. We conclude that both the energy absorbing and the Clayton-Engquist boundary conditions give significantly smaller errors than the simple Dirichlet boundary condition.

### 4.3 Lamb’s problem with $\lambda \gg \mu$

Lamb’s problem has a complicated analytic solution for homogeneous materials with  $\lambda \neq \mu$ , see [13]. Since we are interested in the accuracy of the far-field boundary conditions, it suffices to study the numerical solution at a time  $T$  when the exact solution is identically zero in the computational domain. The solution is dominated by the Rayleigh surface wave and we focus our attention on the error along the surface  $z = 0$ . As before, we solve Lamb’s problem on the truncated domain  $0 \leq x \leq 12$ ,  $0 \leq y \leq 12$ ,  $0 \leq z \leq 6$  with the point force located at  $\mathbf{x}_0 = (6, 6, 0)$ . The corners of the  $z = 0$  plane are at a distance  $6\sqrt{2}$  from the point force. The phase velocity of the Rayleigh surface wave,  $c_r$ , follows as the real solution of

$$(2 - \xi^2)^2 - 4\sqrt{\left(1 - \left(\frac{c_s}{c_p}\right)^2 \xi^2\right)(1 - \xi^2)} = 0, \quad 0 < \xi = \frac{c_r}{c_s} < 1.$$

Since  $c_r > 0.9$  for  $c_p/c_s \geq \sqrt{3}$ , and  $g(t) = 0$  for  $t \geq 1$ , all waves in the exact solution have propagated out of the  $z = 0$  surface of the computational domain after the time

$$T = 1 + \frac{6\sqrt{2}}{0.9} \approx 10.43.$$

To be consistent with the numerical experiments in the previous section, we evaluate the numerical solution at  $t = 11$ , see Table 3. All three boundary conditions behave similarly to the case with  $c_p/c_s = \sqrt{3}$ , i.e., the error is essentially independent of the grid size, with a significantly smaller error for the two far-field conditions compared to the Dirichlet condition. However, in this case, the error is smaller for the energy absorbing

$h$	Minimal CE	Energy Absorbing	Dirichlet
0.04	0.00874	0.00182	0.02362
0.02	0.00528	0.00190	0.03416

Table 3: Max errors in the  $w$  component of the solution along the surface  $z = 0$  for Lamb’s problem when  $c_p/c_s = 10$  at time 11, after all waves in the exact solution have exited the computational domain.

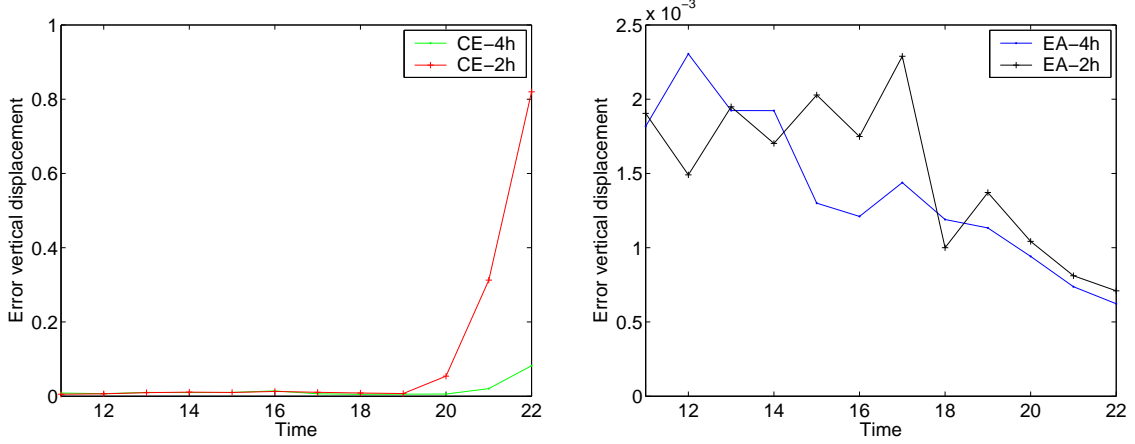


Figure 9: Evolution of the error along the  $z = 0$  surface for  $11 \leq t \leq 22$ , for the Clayton-Engquist (left) and the energy absorbing (right) far field boundary conditions. Here,  $c_p/c_s = 10$  and the two curves correspond to  $h = 0.02$  and  $h = 0.04$ , respectively. Note that the vertical scale goes from 0 to 1 in the left plot, but from 0 to  $2.5 \times 10^{-3}$  in the right plot.

condition than the Clayton-Engquist condition. To investigate what happens as the solution is integrated further in time, we plot the evolution of the maximum norm error of the  $w$  component in Figure 9. We see that the error starts growing rapidly after  $t \approx 19$  when the Clayton-Engquist condition is used. A closer examination of the solution along the line  $z = 0$ ,  $y = 6$  at  $t = 22$  shows a highly oscillatory error for the Clayton-Engquist condition, while the error is smooth for the energy absorbing condition, see Figure 10. We conclude that the Clayton-Engquist far-field condition is unstable for  $c_p/c_s = 10$ .

## 5 Conclusions

We have derived an outflow boundary condition for the elastic wave equation which is stable for heterogeneous materials having all ratios of  $c_p/c_s$ . An energy estimate has been derived for the fully discretized equations, proving that the proposed boundary condition is energy absorbing when the explicit time-step satisfies a Courant condition. The stability proof includes edges and corners in a three-dimensional computational domain where several outflow boundaries meet. The stability proof also extends to the case where free

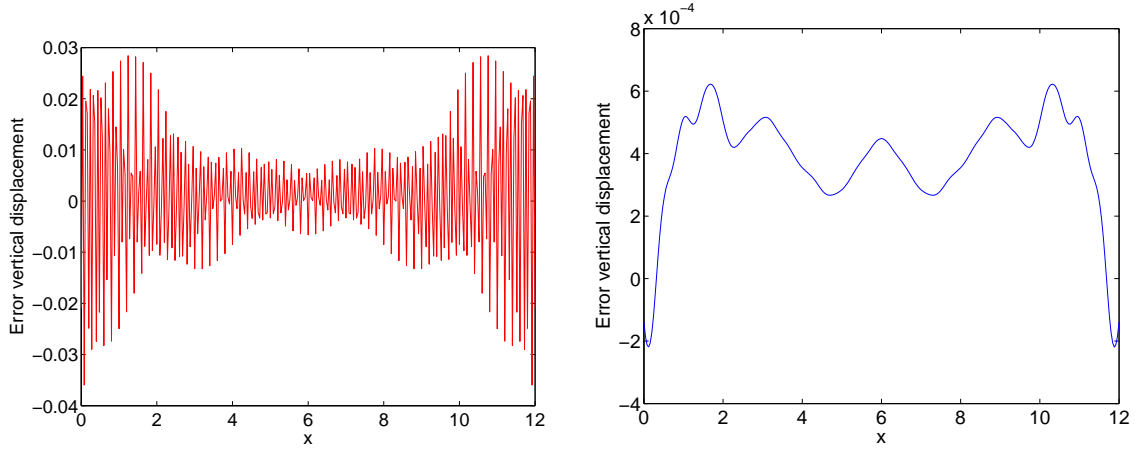


Figure 10: The error along the line  $z = 0$ ,  $y = 6$  at  $t = 22$ , for the Clayton-Engquist (left) and the energy absorbing (right) far field boundary conditions. Here,  $c_p/c_s = 10$  and  $h = 0.04$ . Note that the vertical scale goes from  $-0.04$  to  $0.03$  in the left plot, but from  $-4 \times 10^{-4}$  to  $8 \times 10^{-4}$  in the right plot.

surface boundary conditions are imposed on some sides of the computational domain.

The main advantage of the proposed non-reflecting boundary condition is its guaranteed stability property for heterogeneous materials. The proposed boundary condition is first order accurate in the incident wave angle, and it would be desirable to generalize the energy absorbing principle to derive an outflow boundary condition with improved transmission properties for larger angles of incidence. Prepared by LLNL under Contract DE-AC52-07NA27344.

## References

- [1] D. Appelö and G. Kreiss. A new absorbing layer for elastic waves. *J. Comput. Phys.*, 215:642–660, 2006.
- [2] J. P. Berenger. A perfectly matched layer for the absorption of electromagnetic waves. *J. Comput. Phys.*, 114:185–200, 1994.
- [3] Thomas M. Brocher. Compressional and shear wave velocity versus depth in the San Francisco bay area, California: Rules for USGS bay area velocity model 05.0.0. Technical report, USGS Open-File Report 2005-1317, 2005.
- [4] Robert Clayton and Björn Engquist. Absorbing boundary conditions for acoustic and elastic wave equations. *Bulletin of the Seismological Society of America*, 67, 1977.
- [5] S. M. Day, J. Bielak, D. Dreger, S. Larsen, R. Graves, A. Pitarka, and K. B. Olsen. Tests of 3D elastodynamic codes: Lifelines program task 1A01. Technical report, Pacific Earthquake Engineering Center, 2001.
- [6] Björn Engquist. One way elastic wave equations. Technical Report SEP 10, Stanford University, 1976.



- [7] A. Cemal Eringen and Erdoğan S. Şuhubi. *Elastodynamics, Volume II*. Elsevier, 1975.
- [8] Robert L. Higdon. Radiation boundary conditions for elastic wave propagation. *SIAM J. Numer. Anal.*, 27:831–870, 1990.
- [9] Robert L. Higdon. Absorbing boundary conditions for acoustic and elastic waves in stratified media. *Journal of Computational Physics*, 101, 1992.
- [10] D. Komatitsch and J. Tromp. A perfectly matched layer absorbing boundary condition for the second-order seismic wave equation. *Geophys J. Int.*, 154:146–153, 2003.
- [11] Horace Lamb. On the propagation of tremors over the surface of an elastic solid. *Phil. Trans. Roy. Soc. London, Ser. A*, 203, 1904.
- [12] Kenneth D. Mahrer. An empirical study of instability and improvement of absorbing boundary conditions for the elastic wave equation. *Geophysics*, 51:1499–1501, 1986.
- [13] Harold M. Mooney. Some numerical solutions for Lamb’s problem. *Bulletin of the Seismological Society of America*, 64, 1974.
- [14] S. Nilsson, N. A. Petersson, B. Sjögreen, and H.-O. Kreiss. Stable difference approximations for the elastic wave equation in second order formulation. *SIAM J. Numer. Anal.*, 45:1902–1936, 2007.
- [15] N.A. Petersson, A. J. Rodgers, and B. Sjögreen. User’s guide to the Wave Propagation Program (WPP) version 1.2. Technical Report SM-230257, Lawrence Livermore National Laboratory, 2008. (Source code available from <https://computation.llnl.gov/casc/serpentine>).
- [16] B. Sjögreen and N. A. Petersson. Perfectly matched layers for Maxwell’s equations in second order formulation. *J. Comput. Phys.*, 209:19–46, 2005.
- [17] E. A. Skelton, S. D. M. Adams, and R. V. Craster. Guided elastic waves and perfectly matched layers. *Wave Motion*, 44:573–592, 2007.

## A Proof of Lemma 1

In one space dimension we define the scalar products

$$(u, v)_{1h} = h \sum_{i=1}^N a_i u_i v_i, \quad (u, v)_{1m} = h \sum_{i=1}^{N-1} u_i v_i, \quad (u, v)_{1r} = h \sum_{i=2}^{N-1} u_i v_i.$$

Here  $a_i = 1$  for  $i = 2, 3, \dots, N - 1$ , but  $a_i = 1/2$  for  $i = 1$  and  $i = N$ . The proof of Lemma 1 relies on the application of the identities

$$\begin{aligned} (u, D_- E_{1/2}(\mu) D_+ v)_{1h} &= -(D_+ u, E_{1/2}(\mu) D_+ v)_{1m} \\ &\quad - \frac{1}{2} u_1 (\mu_{1/2} D_+ v_0 + \mu_{3/2} D_+ v_1) + \frac{1}{2} u_N (\mu_{N+1/2} D_+ v_N + \mu_{N-1/2} D_+ v_{N-1}), \end{aligned} \quad (30)$$

$$(u, D_- E_{1/2}(\mu) D_+ v)_{1h} = -(\widetilde{D}_0 u, \mu \widetilde{D}_0 v)_{1h} - \frac{h^2}{4} (D_+ D_- u, \mu D_+ D_- v)_{1r} \\ - \frac{1}{2} u_1 (\mu_{1/2} D_+ v_0 + \mu_{3/2} D_+ v_1) + \frac{1}{2} u_N (\mu_{N+1/2} D_+ v_N + \mu_{N-1/2} D_+ v_{N-1}), \quad (31)$$

and

$$(u, \widetilde{D}_0 v)_{1h} = -(\widetilde{D}_0 u, v)_{1h} - u_1 v_1 + u_N v_N, \quad (32)$$

along each of the coordinate directions. We have

$$(\mathbf{u}^1, \mathbf{L}(\mathbf{u}^0))_h = (u^1, L^{(u)}(u^0, v^0, w^0))_h + (v^1, L^{(v)}(u^0, v^0, w^0))_h + (w^1, L^{(w)}(u^0, v^0, w^0))_h, \quad (33)$$

and we proceed by making a detailed analysis of the first term on its right hand,

$$(u^1, L^{(u)}(u^0, v^0, w^0))_h = (u^1, D_-^x (E_{1/2}^x (2\mu) D_+^x u^0))_h + (u^1, D_-^x (E_{1/2}^x (\lambda) D_+^x u^0))_h \\ + (u^1, D_-^y (E_{1/2}^y (\mu) D_+^y u^0))_h + (u^1, D_-^z (E_{1/2}^z (\mu) D_+^z u^0))_h \\ + (u^1, \widetilde{D}_0^x (\lambda \widetilde{D}_0^y v^0 + \lambda \widetilde{D}_0^z w^0))_h + (u^1, \widetilde{D}_0^y (\mu \widetilde{D}_0^x v^0))_h + (u^1, \widetilde{D}_0^z (\mu \widetilde{D}_0^x w^0))_h. \quad (34)$$

We use relation (30) in the  $x$ -direction on the first term in the right hand side of (34). The second, third, and fourth terms are rewritten by using (31) in the  $x$ -,  $y$ -, and  $z$ -coordinate directions, respectively. For the fifth, sixth, and seventh terms we use the summation by parts property (32) in the  $x$ -,  $y$ -, and  $z$ -directions, respectively. These manipulations lead to

$$(u^1, L^{(u)}(u^0, v^0, w^0))_h = -2(D_+^x u^1, E_{1/2}^x (\mu) D_+^x u^0)_{mx} \\ - \frac{h^2}{4} [(D_+^x D_-^x u^1, \lambda D_+^x D_-^x u^0)_{rx} + (D_+^y D_-^y u^1, \mu D_+^y D_-^y u^0)_{ry} + (D_+^z D_-^z u^1, \mu D_+^z D_-^z u^0)_{rz}] \\ - (\widetilde{D}_0^x u^1, \lambda (\widetilde{D}_0^x u^0 + \widetilde{D}_0^y v^0 + \widetilde{D}_0^z w^0))_h - (\widetilde{D}_0^y u^1, \mu \widetilde{D}_0^x u^0)_h - (\widetilde{D}_0^z u^1, \mu \widetilde{D}_0^x u^0)_h \\ - (\widetilde{D}_0^y u^1, \mu \widetilde{D}_0^x v^0)_h - (\widetilde{D}_0^z u^1, \mu \widetilde{D}_0^x w^0)_h \\ + h^2 \sum_{j=1}^{N_y} \sum_{k=1}^{N_z} \left( -u_{1,j,k}^1 (\mathcal{B}_{1,j,k}^0)^{11} + u_{N_x,j,k}^1 (\mathcal{B}_{N_x,j,k}^0)^{11} \right) \\ + h^2 \sum_{i=1}^{N_x} \sum_{k=1}^{N_z} \left( -u_{i,1,k}^1 (\mathcal{B}_{i,1,k}^0)^{12} + u_{i,N_y,k}^1 (\mathcal{B}_{i,N_y,k}^0)^{12} \right) \\ + h^2 \sum_{i=1}^{N_x} \sum_{j=1}^{N_y} \left( -u_{i,j,1}^1 (\mathcal{B}_{i,j,1}^0)^{13} + u_{i,j,N_z}^1 (\mathcal{B}_{i,j,N_z}^0)^{13} \right), \quad (35)$$

where  $(\mathcal{B}_{i,j,k}^0)^{11}$ ,  $(\mathcal{B}_{i,j,k}^0)^{12}$ , and  $(\mathcal{B}_{i,j,k}^0)^{13}$  are defined by (16)-(18). The reduced norm  $(u, v)_{rx}$  is the three-dimensional counterpart of  $(u, v)_{1r}$ , i.e., it is defined like  $(u, v)_h$  but with the sum over  $i$  taken from 2 to  $N_x - 1$  instead of 1 to  $N_x$ . Similarly, the sum over  $j$  in  $(u, v)_{ry}$  is taken from 2 to  $N_y - 1$ , and the sum over  $k$  in  $(u, v)_{rz}$  is taken from 2 to  $N_z - 1$ . Furthermore, we define

$$(u, v)_{mx} = h^3 \sum_{i=1}^{N_x-1} \sum_{j=1}^{N_y} \sum_{k=1}^{N_z} u_{i,j,k} v_{i,j,k}.$$

Similarly, we define  $(u, v)_{my}$  with the sum over  $j$  from 1 to  $N_y - 1$ , and  $(u, v)_{mz}$  with the sum over  $k$  from 1 to  $N_z - 1$ ,

It is not hard to see that the boundary contributions from summation by parts property (32) applied to terms five, six, and seven in (34) give the  $\widetilde{D}_0$  terms in  $(\mathcal{B})^{11}$ ,  $(\mathcal{B})^{12}$ , and  $(\mathcal{B})^{13}$ . The remaining parts of  $(\mathcal{B})^{11}$ ,  $(\mathcal{B})^{12}$ , and  $(\mathcal{B})^{13}$  come from applying (30) to the first term as well as applying (31) to terms two, three, and four.

We rewrite  $(v^1, L^{(v)}(u^0, v^0, w^0))_h$  and  $(w^1, L^{(w)}(u^0, v^0, w^0))_h$  using the same approach as for  $(u^1, L^{(u)}(u^0, v^0, w^0))_h$ . Assembling all terms in the right hand side of (33) gives

$$(\mathbf{u}^1, \mathbf{L}(\mathbf{u}^0))_h = -S_1(\mathbf{u}^1, \mathbf{u}^0) - \frac{h^2}{4}R(\mathbf{u}^1, \mathbf{u}^0) + T(\mathbf{u}^1, \mathbf{u}^0). \quad (36)$$

where  $T(\mathbf{u}^1, \mathbf{u}^0)$  is given by (21) and

$$\begin{aligned} S_1(\mathbf{u}^1, \mathbf{u}^0) = & 2(D_+^x u^1, E_{1/2}^x(\mu) D_+^x u^0)_{mx} + 2(D_+^y v^1, E_{1/2}^y(\mu) D_+^y v^0)_{my} \\ & + 2(D_+^z w^1, E_{1/2}^z(\mu) D_+^z w^0)_{mz} + (\widetilde{D}_0^x u^1 + \widetilde{D}_0^y v^1 + \widetilde{D}_0^z w^1, \lambda(\widetilde{D}_0^x u^0 + \widetilde{D}_0^y v^0 + \widetilde{D}_0^z w^0))_h \\ & + (\widetilde{D}_0^y u^1 + \widetilde{D}_0^x v^1, \mu(\widetilde{D}_0^y u^0 + \widetilde{D}_0^x v^0))_h + (\widetilde{D}_0^z u^1 + \widetilde{D}_0^x w^1, \mu(\widetilde{D}_0^z u^0 + \widetilde{D}_0^x w^0))_h \\ & + (\widetilde{D}_0^z v^1 + \widetilde{D}_0^y w^1, \mu(\widetilde{D}_0^z v^0 + \widetilde{D}_0^y w^0))_h. \end{aligned} \quad (37)$$

The term  $R(\mathbf{u}^1, \mathbf{u}^0)$  is given by

$$\begin{aligned} R(\mathbf{u}^1, \mathbf{u}^0) = & (D_+^x D_+^x u^1, \lambda D_+^x D_+^x u^0)_{rx} + (D_+^y D_+^y u^1, \mu D_+^y D_+^y u^0)_{ry} + (D_+^z D_+^z u^1, \mu D_+^z D_+^z u^0)_{rz} \\ & + (D_+^x D_+^x v^1, \mu D_+^x D_+^x v^0)_{rx} + (D_+^y D_+^y v^1, \lambda D_+^y D_+^y v^0)_{ry} + (D_+^z D_+^z v^1, \mu D_+^z D_+^z v^0)_{rz} \\ & + (D_+^x D_+^x w^1, \mu D_+^x D_+^x w^0)_{rx} + (D_+^y D_+^y w^1, \mu D_+^y D_+^y w^0)_{ry} + (D_+^z D_+^z w^1, \lambda D_+^z D_+^z w^0)_{rz}. \end{aligned} \quad (38)$$

Note that  $S_1$  and  $R$  are symmetric in their arguments. We can therefore group all symmetric contributions of (36) into

$$S(\mathbf{u}^1, \mathbf{u}^0) = S_1(\mathbf{u}^1, \mathbf{u}^0) + \frac{h^2}{4}R(\mathbf{u}^1, \mathbf{u}^0), \quad S(\mathbf{u}^0, \mathbf{u}^1) = S(\mathbf{u}^1, \mathbf{u}^0).$$

Since all terms in  $S(\mathbf{u}, \mathbf{u})$  are non-negative, it is positive semi-definite. Finally, note that due to the restricted norms and the one-sided operators ( $\widetilde{D}_0^x$  etc.) at the boundaries, no ghost points values are used in any of the terms in (37) and (38). This proves Lemma 1.

□